Load partitioning between ferrite and cementite during elasto-plastic deformation of an ultrahigh-carbon steel

M.L. Young [a,b], J.D. Almer [b], M.R. Daymond [c], D.R. Haeffner [b], D.C. Dunand [a,*]

[a] *Department of Materials Science and Engineering, Northwestern University, Evanston, IL 60208, USA*
[b] *Advanced Photon Source, Argonne National Laboratory, Argonne, IL 60439, USA*
[c] *Department of Mechanical and Materials Engineering, Queen's University, Kingston, Ont., Canada K7L 3N6*

Abstract

An ultrahigh-carbon steel was heat-treated to form an in situ composite consisting of a fine-grained ferritic matrix with 34 vol.% submicron spheroidized cementite particles. Volume-averaged lattice elastic strains for various crystallographic planes of the α-Fe and Fe_3C phases were measured by synchrotron X-ray diffraction for a range of uniaxial tensile stresses up to 1 GPa. In the elastic range of steel deformation, no load transfer occurs between matrix and particles because both phases have nearly equivalent elastic properties. In the steel plastic range after Lüders band propagation, marked load transfer takes place from the ductile α-Fe matrix to the elastic Fe_3C particles. Reasonable agreement is achieved between phase lattice strains as experimentally measured and as computed using finite-element modeling.
© 2006 Acta Materialia Inc. Published by Elsevier Ltd. All rights reserved.

1. Introduction

Although steels with high and ultrahigh-carbon content have been produced for many centuries (e.g. Wootz and Damascus steel), their microstructure and mechanical properties have only recently begun to be studied with modern scientific methods [1–7]. These steels have a remarkable combination of mechanical properties, e.g. very high hardness, strength and wear resistance, good ductility, and superplasticity at elevated temperature [1–7]. Ultrahigh-carbon steel (UHCS) is an in situ composite with a high volume fraction of strong, brittle, ceramic particles (Fe_3C, cementite) precipitated by heat treatment within a soft, ductile matrix (α-Fe, ferrite). The UHCS carbon content is in the range 1.0–2.1 wt.% (4.5–9.1 at.%) [4], corresponding to a cementite volume fraction of 15–32% (as determined from the binary Fe–C diagram). Such high vol-

ume fractions of ceramic reinforcement are typical of metal matrix composites (MMCs) produced by ex situ methods [8]. Much research has been devoted to measuring the load partitioning between matrix and reinforcement in MMCs by neutron [9–19] and synchrotron X-ray [20–28] diffraction, and modeling the load transfer based on matrix/reinforcement elastic mismatch, matrix plasticity, interface damage and reinforcement fracture [9–13,15–17,19–22, 24–26,28].

Similar to these ex situ MMCs, the load partitioning between the α-Fe and Fe_3C phases in UHCS has also been studied by diffraction. Using X-ray diffraction, lattice strains for these two phases in spheroidized UHCS (1.1 wt.% C) were first measured by Wilson et al. [29,30] upon mechanical loading and unloading. X-ray microbeam diffraction using laboratory-source X-rays was also used to study the effect of residual stresses in α-Fe and Fe_3C phases in high-carbon steel (0.54–0.8 wt.% C) [31]. However, these results apply only to the near-surface volume due to the low penetration depth of laboratory-source X-rays in iron.

---

* Corresponding author. Tel.: +847 491 5370; fax: +847 491 7820.
E-mail address: dunand@northwestern.edu (D.C. Dunand).

Table 1
Composition and estimated Fe_3C volume fraction for high- and ultrahigh-carbon steels used in previous and present diffraction studies of load transfer

Alloying elements (wt.%)					Fe_3C (vol.%)	Diffraction method
C	Si	Mn	Cr	Al		
0.35–0.40	0.20–0.65	1.30–1.60	0.15	0.03	8	Neutron [32]
0.82	0.23	0.73	–	–	16	Neutron [33]
0.88	0.16	0.51	–	–	17	Neutron [34]
1.0	0.3	0.35	0.4	–	19	Neutron [35]
1.8	–	0.5	1.5	1.6	34	Synchrotron X-rays (present work)

Neutron diffraction, which allows for much higher penetration depths in high-atomic-weight elements such as iron, was recently used to study load transfer between the α-Fe and Fe_3C phases during tensile deformation of high- and ultrahigh-carbon steel samples with 0.35–1 wt.% C [32–35], as summarized in Table 1.

The goal of the present study is to use, for the first time, synchrotron X-ray diffraction to measure bulk phase strains during deformation of a UHCS with very high carbon content (1.8 wt.% C), as a function of applied stress, crystallographic orientation and rolling direction. Measurements of the load transfer between α-Fe and Fe_3C are compared to predictions from a finite-element model and discussed in light of earlier neutron diffraction work [32–35] on steels with lower Fe_3C volume fractions (Table 1).

2. Experimental procedures

2.1. Materials processing

A UHCS with 1.8 wt.% C (see Table 1 for the full composition) was procured from the same stock as the material studied by Taleff et al. [4]. The steel had been heat-treated according to the following schedule: (i) soaking at 1093 °C for 8 h (in the γ-Fe field); (ii) hot-rolling in several steps from 1093 to 900 °C (γ field to γ + Fe_3C field); (iii) hot-shearing into segments; (iv) soaking at 1093 °C for 48 h (in the γ field); and (v) furnace-cooling. In a final step, the ingot had been reheated to 810 °C (γ + Fe_3C field) and warm-rolled continuously to a temperature of about 750 °C (γ + Fe_3 field). The heat-treated and rolled plate was then machined into a tensile sample (shown in

Fig. 1) with a 1.3×1.3 mm^2 gage section and a 15.6 mm gage length, subsequently soaked at 200 °C for 1 h, and finally heat-treated at 950 °C (γ + Fe_3 field) for 20 min in a high-vacuum furnace prior to tensile testing. Here, the final 950 °C heat-treatment was slightly higher than in Ref. [4] where the final heat treatment was performed at 840 or 870 °C. As shown in Table 1, the Fe_3C volume fraction of 34% studied here is almost twice that of the previous neutron experiments. This volume fraction was found by linear extrapolation of those reported in Refs. [32,35] with similar levels of non-C alloying additions, and is higher than the volume fraction calculated by the lever rule (27%) assuming a binary Fe–1.8 wt.% C composition.

2.2. Diffraction measurements

High-energy X-ray diffraction measurements were carried out at the 1-ID beamline of the Advanced Photon Source (Argonne National Laboratory, IL). In situ uniaxial tensile testing was performed using a custom-built, screw-driven loading system operated in displacement control. The average sample macroscopic stress and strain were recorded with a load cell and a strain gage attached to the sample, respectively. The general setup for these experiments is shown in Fig. 1 and is similar to that used in Refs. [24,25,36–40]. The sample was subjected to increasing uniaxial tensile stresses up to failure, with the stress parallel to the rolling direction. The macroscopic stress and strain were recorded at every 10 μm cross-head displacement increment. At every 50 μm increment, diffraction measurements were performed with a monochromatic 81 keV ($\lambda = 0.015$ nm) X-ray beam for 90 s (this is a much shorter exposure time than with current neutron sources,
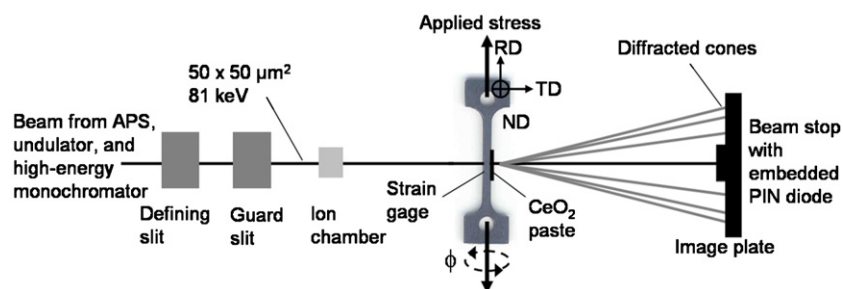

Fig. 1. Schematic of experimental diffraction setup, showing photograph of a UHCS tensile sample with rolling (RD), transverse (TD) and normal (ND, out of the page) directions indicated.

thus ensuring that sample creep during the experiment was negligible). The incident X-ray beam, with a square 50×50 μm² cross-section, was positioned in the center of the specimen cross-section and was parallel to either the normal direction (ND) or the transverse direction (TD) with respect to the rolling plane, dependent on the orientation of the sample. Complete Debye–Scherrer diffraction rings from the α-Fe matrix and the Fe₃C reinforcement present in the diffraction volume were recorded using an image plate (Mar345) with 345 mm diameter, operating in full mode and providing a pixel size of 100 μm with 16 bit dynamic range. An ion chamber and a PIN diode (p-type, intrinsic, n-type diode) embedded within the beam stop were used to measure the initial and transmitted beam intensity, respectively, thus facilitating sample positioning with respect to the beam. The sample-to-camera distance was 1.036 m. In addition, calibration diffraction cones were produced from a paste composed of vacuum grease and pure ceria powder (CeO₂, NIST Standard Reference Material SRM-674a), which was smoothly applied to the surface of the sample (Fig. 1).

2.3. Diffraction analysis

A typical diffraction pattern is shown in Fig. 2. As evidenced by the high uniformity of the diffraction ring intensities, the Fe₃C particles and the α-Fe grains are significantly smaller than the $50 \times 50 \times 1300$ μm³ diffracting volume. To determine the lattice strains from measured diffraction rings, an algorithm similar to those from Refs. [25,41,42] was used, which takes into account the whole diffraction rings. This algorithm is implemented using the program language MATLAB [43], and consists of the following steps:

1. The beam center, detector tilt and sample-to-detector distance ('calibration parameters') are determined with the software FIT2D [44,45], using CeO₂ (2 0 0) reflections near the center and CeO₂ (3 3 3) reflections near the outer edge of the detector.

2. The diffraction pattern is converted from polar to Cartesian coordinates in N radial $\times M$ azimuthal bins (typically with values of $N = 800$, corresponding to 2.2 pixels, and $M = 144$, corresponding to an angle increment of 2.5°), using the calibration parameters to correct for beam center, detector tilt and sample-to-detector distance.

3. For selected crystallographic reflections, the profile of the peak intensity as a function of radial distance is fitted using a pseudo-Voigt function to find the average center of the peak intensity R. This is done for all M azimuthal bins (i.e. in angle increments of $\eta = 2.5°$).

4. The $R(\eta)$ values are converted to absolute d-spacings $d(\eta)$ using the above calibration parameters, in addition to the known X-ray wavelength.

5. Plots of R vs. $\sin^2(\psi)$ are created for all applied stress, where $\psi = \eta + \theta \cos(\eta)$ (with θ as the Bragg angle and $0 < \eta < \pi/2$ and similar relationships given in Ref. [41] for $\pi/2 < \eta < 2\pi$). The resulting lines intersect at an invariant "strain-free" value R_0 and invariant azimuthal angle η_0.

6. The X-ray lattice strain for a given (hkl) reflection is calculated using:

$$\varepsilon(\eta) = \frac{(R_0 - R(\eta))}{R_0} \qquad (1)$$

and these values are then used to determine the two axial strain components in the sample coordinate system ($e_{11} = \varepsilon(90°)$ and $e_{22} = \varepsilon(0°)$) using equations derived by He and Smith [46] for two-dimensional detectors.

3. Results

3.1. Steel microstructure and stress–strain curve

Optical micrographs of the sample etched with 2% Nital revealed a fine-grained α-Fe matrix with a high volume fraction of fine, spheroidized Fe₃C particles, as depicted in Fig. 3a. Also present as a minority phase was proeutectoid Fe₃C oriented in large striations exceeding 1 mm in length. Scanning electron microscopy of the etched sample was used to resolve the fine, micrometer-size Fe₃C spheroids embedded within the α-Fe matrix (Fig. 3b). While image analysis had too much error to provide useful results, Fig. 3b shows that the calculated Fe₃C volume fraction of 34% is realistic.

Before loading the sample, synchrotron X-ray diffraction measurements were taken from $\phi = 0°$ (ND) to 90° (TD), Fig. 1, in 5° increments, and pole figures were created to determine the initial texture, as shown in Fig. 4a and b. These pole figures show that the α-Fe (2 0 0) reflections are
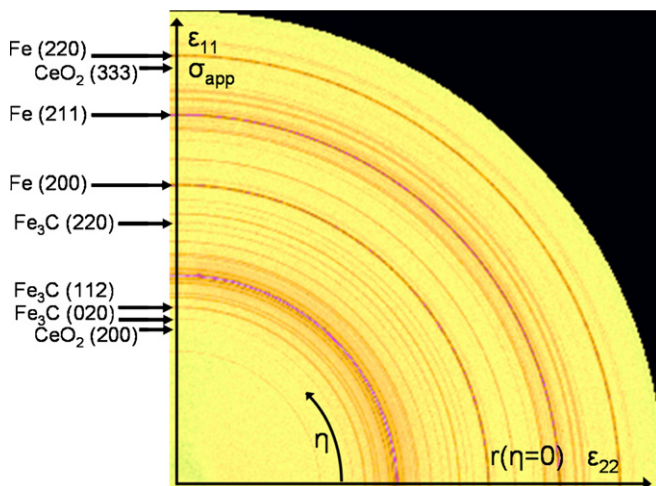

Fig. 2. Representative X-ray diffraction pattern (quarter of image plate) of the UHCS sample. All of the diffraction rings were identified. For clarity, only some of the rings belonging to CeO₂, α-Fe, and Fe₃C phases are indicated here. Darker pixels indicate higher diffracted intensity.
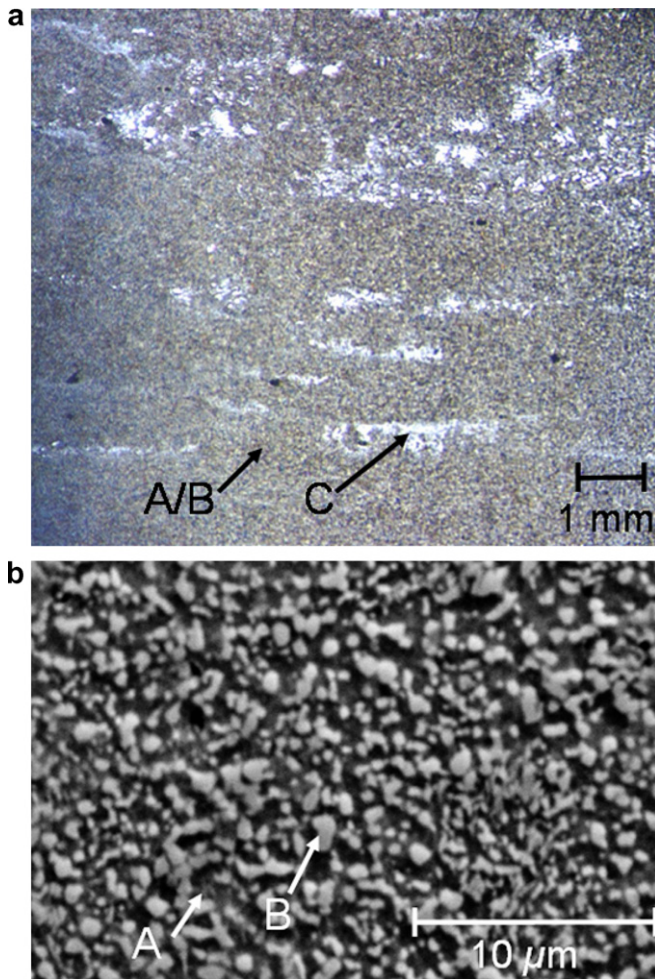
Fig. 3. (a) Optical micrograph of the UHCS sample etched with 2% Nital showing a region of α-Fe matrix and Fe₃C spheroids (A/B) and large striations of proeutectoid Fe₃C (C). (b) Scanning electron micrograph in secondary electron mode of a UHCS sample etched with 2% Nital with α-Fe matrix (A) and Fe₃C spheroids (B) indicated.

preferentially oriented in the rolling direction, while the α-Fe (2 1 1) reflections are preferentially oriented at an intermediate angle between the rolling and transverse directions, which is in general agreement with results from
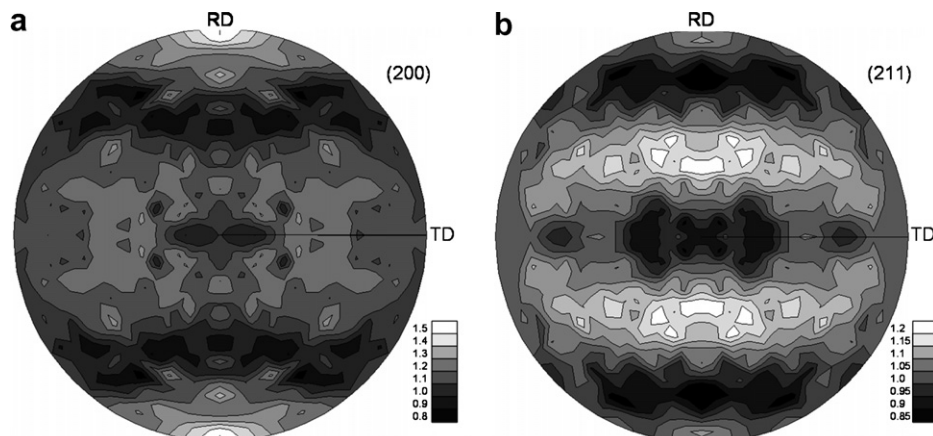
previous studies on low-carbon and duplex steels [47–49]. The texture due to rolling was weak, as the maximum multiple random distribution (MRD) values of 1.5 and 1.2 for the α-Fe (2 0 0) and (2 1 1) reflections, respectively, are close to unity (corresponding to a perfectly isotropic material).

The macroscopic stress–strain curve for the UHCS sample is shown in Fig. 5. Upon initial loading, elastic behavior with a Young's modulus of 204 GPa was exhibited up to a stress of 720 MPa, where yielding occurred by Lüders band nucleation and propagation over a macroscopic sample strain of 0.7%. This was followed by plastic deformation with strain hardening up to failure at a stress of 1060 MPa and an engineering strain of 6.1%.

3.2. Phase lattice strain evolution

The lattice parameter value for pure body-centered cubic α-Fe (pdf # 06-0696) is $a = 2.866$ Å [50], which is slightly smaller (by ∼0.2%) than the iterative value of 2.871 Å determined for the α-Fe in this study. The lattice parameter values for orthorhombic Fe₃C (pdf # 85–0871) are $a = 4.51$, $b = 5.04$, and $c = 6.73$ Å [51], which are also slightly smaller than, but within error of, the iterative values of 4.515, 5.08, and 6.77 Å, respectively, determined for the Fe₃C in this study. Such differences in absolute lattice parameters are often found due to minor alloying variations, but do not have an impact on the strains measured, which are based on relative variation in lattice parameter.

As illustrated in Fig. 6a and b, the lattice strain vs. $\sin^2 \psi$ plots for the Fe (2 2 0) reflection were linear in the steel elastic range and nonlinear in the plastic range. For the Fe₃C (2 2 0) reflection, these plots were linear throughout the whole loading range, as shown in Fig. 6c where, for clarity, only one out of every three curves is plotted. The "strain-free" lattice spacing for the α-Fe (2 2 0) and Fe₃C (2 2 0) reflections are $d_0 = 1.0160$ Å and 0.3534 Å, respectively, as illustrated in Fig. 6a and c.

Fig. 7 shows plots of applied stress vs. lattice strain (e_{11} and e_{22} in directions axial and transverse to loading, respectively), as calculated from diffraction measurements for the α-Fe (2 2 0) and Fe₃C (2 2 0) reflections. At zero

Fig. 4. Pole figures with no applied stress for the (a) (2 0 0) and (b) (2 1 1) α-Fe reflections. Scale shows MRD values.
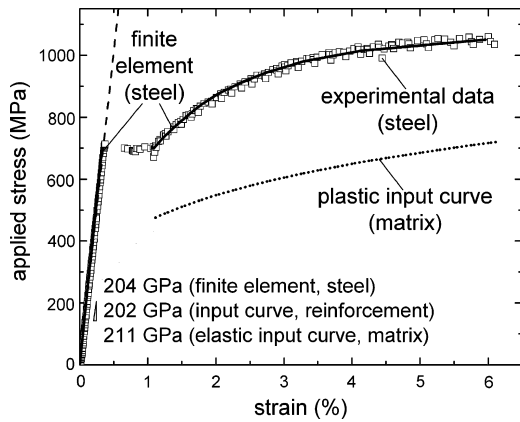
Fig. 5. Macroscopic stress–strain curve for UHCS tensile sample showing experimental data (open squares), α-Fe and Fe₃C reinforcement elastic input curve (dashed line), α-Fe matrix plastic input curve (dotted line), and steel curve calculated from finite-element model (solid line). The model does not capture the Lüders band propagation between the elastic and plastic ranges.

applied stress, residual strains are near zero. In the steel elastic range, the slopes for the α-Fe matrix (209 GPa) and the Fe₃C reinforcement (229 GPa) in the axial direction are, within experimental error, equal to each other and to the macroscopic Young's modulus for the steel (204 GPa). Similarly, the slopes for the α-Fe matrix (−739 GPa) and the Fe₃C reinforcement (−689 GPa) in the transverse direction to loading (e_{22}) are equal within experimental error (these slopes are negative due to the compressive nature of transverse strains). The absolute value of the ratio of these slopes gives Poisson's ratios of $v = 0.28$ and 0.33 for α-Fe and Fe₃C, respectively, in good agreement with the literature values of 0.29 for both phases [52,53]. While the lattice strains are the same for both phases in the elastic range of the steel deformation, they are vastly different in the plastic range: immediately after yield by Lüders band propagation, the matrix lattice strains (both axial and transverse) drop well below the maximum value observed in the elastic range, while the Fe₃C strains rise well above their elastic value. The Fe₃C reinforcement displays an axial strain higher by a factor of 2.4 (at the beginning of the plastic range) to 3.6 (at fracture), as compared to the Fe matrix (Fig. 7). Such load shedding from matrix to reinforcement is characteristic of MMCs displaying elastic reinforcement in a plastic matrix [9–28,54–56].

The strain evolution of both phases, using the α-Fe (2 2 0) and Fe₃C (2 2 0) reflections, is shown in Fig. 8a and b for two orthogonal directions relative to the rolling direction. For the Fe₃C reinforcement, a small amount of residual strain (250 με) is present before loading. In the steel elastic range, the stress vs. lattice strain slopes for each phase are equivalent for both directions, within experimental error. In the steel plastic range, however, load transfer from matrix to reinforcement is more pronounced in the normal direction than in the transverse direction. Such a direction-dependent behavior in the steel plastic range is not observed, within experimental error, for the Fe₃C phase.
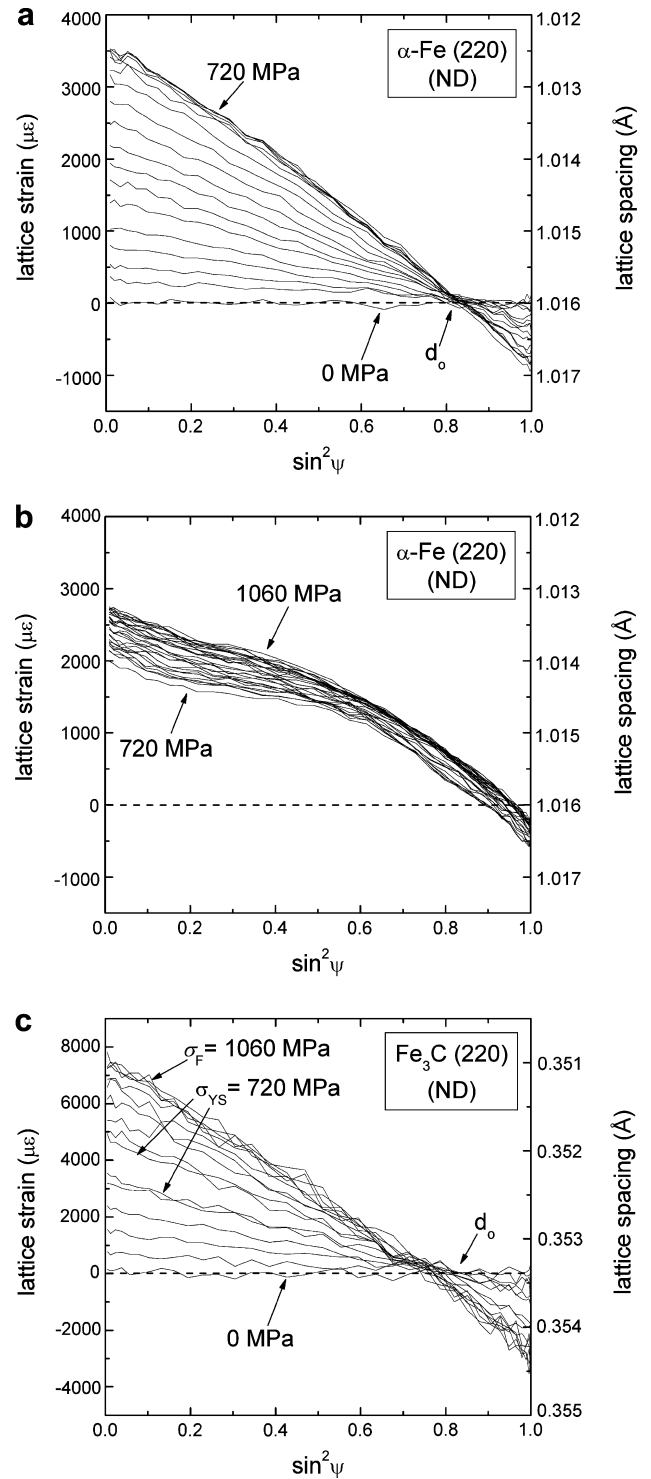

Fig. 6. Lattice strain/lattice spacing vs. $\sin^2 \psi$ distributions for (a) the α-Fe matrix in the elastic steel range; (b) the α-Fe matrix in the plastic steel region, and (c) the Fe₃C particles in the elastic and plastic steel ranges. Each line represents a single diffraction ring from the Fe (2 2 0) and Fe₃C (2 2 0) reflections, respectively, at a unique stress. For the Fe₃C (2 2 0) reflection, only one out of every three diffraction rings is shown. No applied stress (0 MPa), the onset and end of the Lüders band (∼720 MPa), and the highest stress before failure (1060 MPa) are indicated in the figures.

The anisotropic response of individual lattice reflections is illustrated in Fig. 9a, which shows the α-Fe (2 0 0), (2 2 0), and (2 1 1) reflections, corresponding to three different sets of
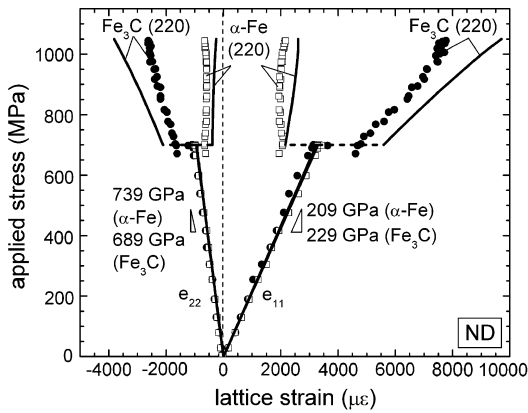
Fig. 7. Applied stress vs. lattice strain (e_{22} perpendicular and e_{11} parallel to the applied stress) for the α-Fe (220) and Fe_3C (220) reflections for sample oriented with rolling in the ND parallel to beam. The values of the slopes for the α-Fe (220) and Fe_3C (220) reflections are based on best fit of the experimental data. Error bars are too small to be represented, with typical strain uncertainties of 40 $\mu\varepsilon$. Average elastic strains from finite-element modeling are shown as solid lines (dashed lines in the Lüders region are shown for continuity).

matrix grains oriented with their respective crystallographic direction parallel ($\eta = 90°/270°$) or perpendicular ($\eta = 0°/180°$) to the applied stress. In the steel elastic range, the α-Fe (200) axial slope (155 GPa) is significantly lower than those for the (220) and (211) reflections (209 and 206 GPa, respectively); a similar effect is found for transverse strains. In the plastic range, anisotropy is also present: less load is transferred to the Fe_3C phase from the grains producing the α-Fe (200) reflection than from those producing the (220)/(211) reflections, in both the axial and transverse directions. The applied stress vs. lattice strain curves for the (220) and (211) reflections show almost identical behavior. These results are consistent with previous reports [32,35] and reflect the typical elastic and plastic behavior of iron.

Fig. 9b shows the anisotropic response of the Fe_3C (020), (220) and (112) reflections. In the steel elastic range, no significant anisotropic effects are observed with slopes for the three crystallographic reflections equal, within experimental error, for both transverse and axial strains. In the plastic range, more load transfer occurs to the Fe_3C (112) and (020) reflections than to the (220) reflection. Other crystallographic planes for both phases were recorded and fall within the range of the reflections shown in Fig. 9a and b, and therefore are not presented here.

3.3. Finite-element modeling

Unit-cell three-dimensional (3D) finite-element modeling has been shown to be a powerful method for investigating load sharing between phases in MMCs (see e.g., Refs. [57–68]). The present study used the ABAQUS software package (version 6.5 with Computer Aided Engineering, CAE, module). Due to symmetry, the system can be modeled as one-eighth of a α-Fe cube containing a Fe_3C sphere, with dimensions chosen to achieve a Fe_3C volume fraction
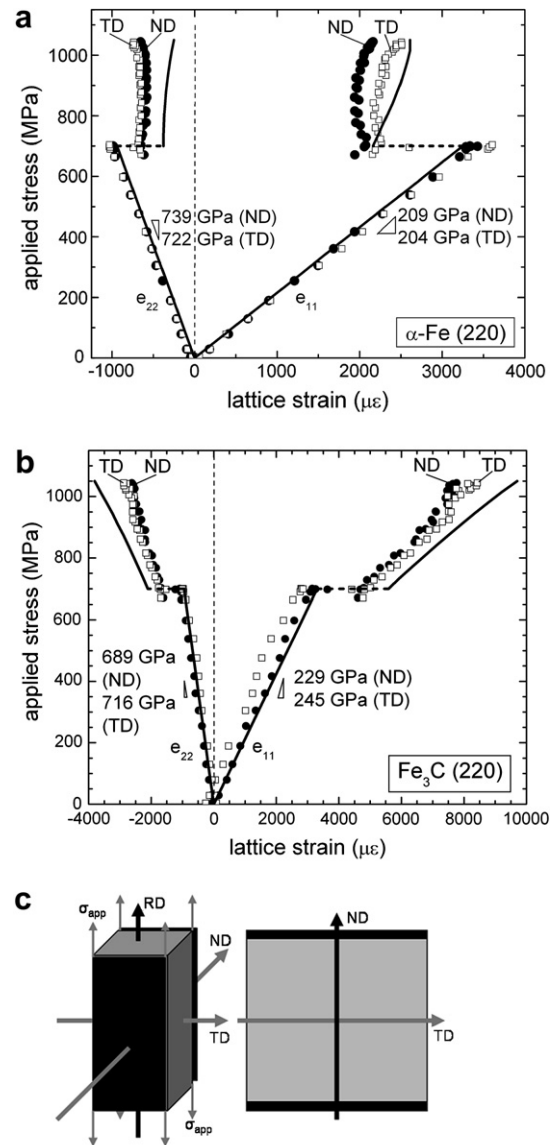

Fig. 8. Applied stress vs. lattice strain (e_{22} perpendicular and e_{11} parallel to the applied stress) for beams parallel to ND and TD for (a) the α-Fe (220) reflection and (b) the Fe_3C (220) reflection. The values of the slopes in the elastic range represent best fit of the experimental data. Average elastic strains from finite-element modeling are shown as solid lines (dashed lines in the Lüders region are shown for continuity). (c) Schematic of sample orientation with respect to tensile stress. The beam is parallel to either ND or TD, and stress is always parallel to RD.

of 34%. Infinite, periodic boundary conditions with mirror planes were applied, thus simulating an infinite cubic array of Fe_3C spheres embedded within the α-Fe matrix. The total number of elements (C3D20: 3D cubic quadratic elements with 20 nodes each) was 2079 for the Fe matrix and 2591 for the Fe_3C particle. The lower plane of the model is constrained in the vertical direction, with one corner fully constrained to prevent overall model translation due to numerical round-off errors. A tensile force is applied to each node on the top of the structure, simulating a uniform stress. The Young's modulus E and Poisson's ratio v used for the two phases were: $E_{\alpha-Fe} = 211$ GPa, $v_{\alpha-Fe} = 0.29$
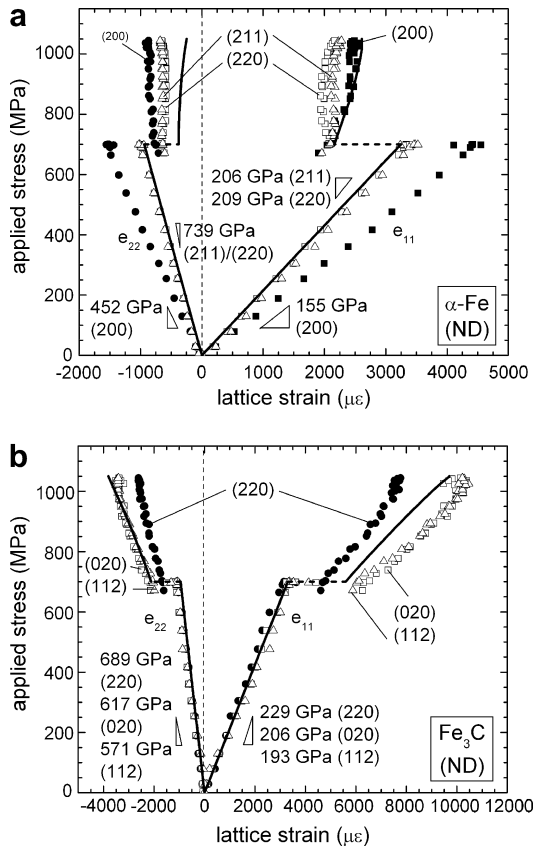
Fig. 9. Applied stress vs. lattice strain for (a) the α-Fe (200), (220) and (211) reflections, and (b) the Fe_3C (020), (220) and (112) reflections, for beams parallel to the ND. The values of the slopes represent best fit of the experimental data. Average elastic strains from finite-element modeling are shown as solid lines (dashed lines in the Lüders region are shown for continuity).

[52] and $E_{Fe3C} = 202$ GPa, $v_{Fe3C} = 0.29$ [52,53], accounting for the slight increase in Young's modulus of the Fe_3C (for pure Fe_3C, $E_{Fe3C} = 196$ GPa and $v_{Fe3C} = 0.29$) due to the additions of 1.5 wt.% Cr and 0.5 wt.% Mn [53]. The model assumes elastic isotropy, and can thus only give an average response for each of the phases.

The model was loaded in tension elastically up to 700 MPa. A user-defined subroutine was used to read axial and transverse strain values at each node, from which a volume-averaged strain value was calculated for each of the two phases. As expected from their very similar elastic constants, the lattice strains of the two phases are almost the same, and are in good agreement with the measured phase strains in the steel elastic range (Fig. 7). The steel finite-element Young's modulus also agrees with the measured value (Fig. 5). The early stage of the steel plastic range cannot be modeled with our simple unit-cell approach, since it is dominated by a local plastic instability (Lüders band) propagating along the sample length. The following procedure was used to address this limitation. Once stress applied on the model reached 700 MPa (very near the experimental yield stress of 720 MPa), the applied stress was held constant at 700 MPa while the strain was increased to 1.1% (corresponding to the end of the Lüders range in Fig. 5). After Lüders band propagation, the matrix plasticity was specified to initiate at a lower stress value of 474 MPa. This behavior corresponds physically to an upper yield stress of 700 MPa and a lower yield stress of 474 MPa. Beyond the lower yield stress, the matrix stress increased due to strain hardening (dotted line in Fig. 5), resulting in an increase in the steel stress until an average strain of 6.1% was reached, corresponding to the failure of the UHCS sample.

To determine the in situ matrix stress–strain curve, the plastic range of the experimental UHCS stress–strain curve was first fitted to a power-law hardening equation [69]:

$$\sigma_T = K\varepsilon_T^n, \tag{2}$$

where σ_T is the true stress, ε_T is the true strain, K is the strength coefficient and n is the strain-hardening exponent. A good fit was reached with K and n values of 1490 MPa and 0.115, respectively. These values were then used as the starting point for determining the lower yield limit of the matrix. An iterative process was used to find α-Fe
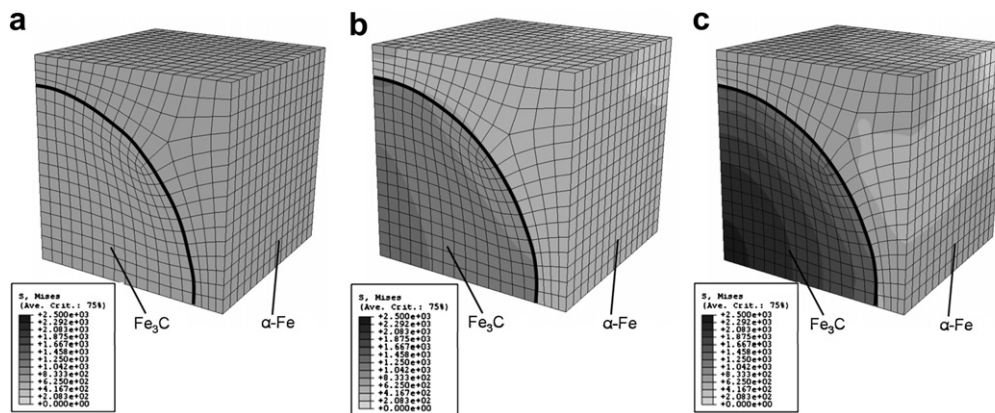

Fig. 10. Finite-element model showing the von Mises stress distribution (a) before Lüders band propagation at 700 MPa; (b) after Lüders band propagation at 700 MPa, and (c) at a maximum load of 1100 MPa. One-eighth of the Fe_3C sphere and the surrounding α-Fe matrix are shown.

matrix values for K and n, until the model-generated macroscopic steel curve agreed well with the experimental UHCS stress–strain curve (Fig. 5). With these matrix parameters fixed at their best-fit values of $K = 1424$ MPa and $n = 0.244$, the volume-averaged strain values were calculated for each phase, using a user-defined subroutine to read axial and transverse strain values at each node of the model. These average phase strains in the plastic range of the steel are plotted as solid lines in Figs. 7–9. It is apparent that, with only two adjustable parameters (K and n) for the strain-hardening behavior of the matrix, reasonable agreement is achieved over the whole steel plastic range for both phases and for both transverse and axial strains.

Fig. 10a–c shows the von Mises stress distribution predicted by the finite-element model at the end of the elastic range just before Lüders band propagation (700 MPa applied stress), at the beginning of the plastic range just after Lüders band propagation (700 MPa applied stress), and at the end of the plastic range for the maximum applied stress of 1100 MPa, respectively. Load transfer from matrix to reinforcement is apparent in the plastic range, and is clearly more pronounced at the higher stress of 1100 MPa. Stresses are also not uniformly distributed within each phase, with stress concentrations visible in the center of the particle and at the matrix/particle interface.

4. Discussion

4.1. Macroscopic tensile behavior

A UHCS with the same composition as the one studied here, which had been subjected to a lower final heat-treatment temperature in the study by Taleff et al. [4], exhibited a higher yield stress (900–1100 MPa) and more extensive Lüders band strain, probably because of its finer cementite size. Comparing the present UHCS with other high- and ultrahigh-carbon steels studied by neutron diffraction by previous researchers (Table 1) [32–35], it is apparent that the yield stress of the present UHCS with 1.6 wt.% C ($\sim$720 MPa) is within the broad range of values reported for the other steels: $\sim$450 MPa for 0.4 wt.% C [32], $\sim$580 MPa for 1.0 wt.% C [35], $\sim$800 and $\sim$1400 MPa for 0.82 wt.% C (as-patented and swaged-annealed, respectively) [33], and $\sim$2400 MPa for a heavily drawn 0.88 wt.% C steel [34]. The broad range of yield stress values is due to both varying carbon content and different processing history, in particular the presence or absence of cold-work. The UHCS studied here failed at 1060 MPa after 6.1% strain, which is within the broad range of previous results $\sim$700 MPa at $\sim$3.5% [32], $\sim$750 MPa at $\sim$8.5% [35], $\sim$900 MPa at $\sim$12% and $\sim$1300 MPa at $\sim$8% (as-patented and swaged-annealed, respectively) [33], and 1100–1300 MPa at 3–11% [4]).

4.2. Phase lattice strains in the steel elastic range

Unlike most MMCs [9–28,54–56], the matrix and reinforcement in carbon steels show near-zero elastic mismatch: the polycrystalline Young's moduli are 211 and 202 GPa for α-Fe and Fe_3C, respectively, and the average Poisson's ratio is 0.29 for both phases [32,53]. Thus, load transfer between the two phases is expected to be insignificant in the elastic range of the stress–strain curve, as is indeed observed in Fig. 7 and in previous neutron experiments on high- and ultrahigh-carbon steels with lower Fe_3C content [32–35].

4.3. Phase lattice strains and stresses in the steel plastic range

After macroscopic yielding has occurred in the UHCS sample, marked load transfer from the ductile α-Fe matrix to the brittle, elastic Fe_3C reinforcement is apparent (Fig. 7). This can be quantified by calculating the average von Mises equivalent stress for each phase, σ_{eff} [57]:

$$\sigma_{eff} = \frac{1}{\sqrt{2}}[(\sigma_{11} - \sigma_{22})^2 + (\sigma_{22} - \sigma_{33})^2 + (\sigma_{33} - \sigma_{11})^2]^{1/2},$$

(3)

where σ_{11} is the axial principal stress, σ_{22} and σ_{33} are the transverse principal stresses, which in turn can be calculated from the measured elastic principal strains ε_{11} and ε_{22} ($=\varepsilon_{33}$) as [57]:

$$\sigma_{11} = \frac{E}{1+v}\varepsilon_{11} + \frac{vE}{(1+v)(1-2v)}(\varepsilon_{11} + \varepsilon_{22} + \varepsilon_{33}), \quad (4a)$$

$$\sigma_{22} = \sigma_{33} = \frac{E}{1+v}\varepsilon_{22} + \frac{vE}{(1+v)(1-2v)}(\varepsilon_{11} + \varepsilon_{22} + \varepsilon_{33}),$$

(4b)

where E is the Young's modulus, and v is the Poisson's ratio of the phase under consideration. Using the measured lattice strains for the Fe (2 2 0) and Fe_3C (2 2 0) reflections and the plane-specific elastic constants [52,53], the effective stresses for the two phases are nearly equal at the highest applied elastic stress of 720 MPa, just prior to yielding ($\sigma_{eff,Fe} = 707$ and $\sigma_{eff,Fe3C} = 663$ MPa). Just after yielding, at the same applied stress of 720 MPa, but after a macroscopic elastic strain of 0.7% corresponding to the end of the Lüders plateau, the phase-effective stresses ($\sigma_{eff,Fe} = 418$ and $\sigma_{eff,Fe3C} = 974$ MPa) now differ by a factor of 2.3. Load transfer continues throughout the steel plastic range up to the last point before fracture (1060 MPa applied stress), where the phase effective stresses have further diverged ($\sigma_{eff,Fe} = 461$ and $\sigma_{eff,Fe3C} = 1626$ MPa), corresponding to a ratio of 3.5. These calculations and the results shown in Fig. 7 demonstrate that, in the steel plastic range, the increase in load-carrying capacity of the steel is almost exclusively accounted for by the Fe_3C phase.

Enhanced load transfer in the plastic range of deformation has also been observed in previous neutron diffraction studies of high- and ultrahigh-carbon steels [32–35] and MMCs [9–28,54–56], where it is explained by the large mismatch developing between the plastically deforming matrix and the elastic reinforcement. Interestingly, the reinforcement size in MMCs is typically 1–2 orders of magnitude larger than in the present UHCS, where the 1 μm size of the Fe_3C particles is close to the critical value below which the dominant strengthening mechanism becomes Orowan strengthening [69]. However, the results presented here clearly indicate that composite strengthening by load transfer in the plastic range of deformation is an important contributor to the strain hardening behavior of this UHCS with its large volume fraction of Fe_3C.

As illustrated in Fig. 6a–c, the lattice strain/spacing vs. $\sin^2 \psi$ plots are near linear for all measured Fe (2 2 0) reflections in the steel elastic range, and for all measured Fe_3C (2 2 0) reflections in both the steel elastic and plastic regions. However, a nonlinear behavior is observed for the Fe (2 2 0) reflections in the plastic region. The linear fit used for these curves to determine matrix lattice strains leads thus to higher errors in the steel plastic range. Similar nonlinear behavior in α-Fe was observed by Hauk et al. [70] using neutrons and laboratory-source X-rays when measuring residual stresses in steels subjected to prior plastic deformations. Various fitting methods have been proposed for nonlinear strain vs. $\sin^2 \psi$ plots [71], but they are not used here as they would affect the calculated strains only marginally given the relatively modest nonlinearity of the curves.

Comparing the strains reported here by synchrotron X-ray diffraction with those measured by neutron diffraction on high- and ultrahigh-carbon steels reported in Refs. [32,35], it is apparent that the load transfer from the α-Fe phase to Fe_3C phase is qualitatively similar but that quantitative differences exist. First, no Lüders band formation is observed in Refs. [32–34], leading to a gradual increase in load transfer from the α-Fe phase to the Fe_3C phase, while in Ref. [35] and the present work, a sharp jump in load transfer is observed after Lüders band propagation has occurred in the diffraction volume. Also, for steels without Lüders band formation, no relaxation of the lattice strains in the α-Fe phase occurs once plasticity initiates. Instead, as the stress increases, the phase strains retain roughly the same value achieved at yield. In contrast, high- and ultrahigh-carbon steels exhibiting Lüders band formation and propagation, as in Ref. [35] and the present investigation, show a distinct reduction in lattice strain for the α-Fe phase and a distinct increase in the Fe_3C phase after Lüders band propagation. However, the exact average phase strain values are sensitive to the number of reflections observed and the geometry of the Fe_3C phase (leading to a different Poisson constraint). The magnitude of the drop in lattice strain for the α-Fe phase is quite similar in the two steels with Lüders bands with ∼900 με (average phase strain) in Ref. [35] with 20 vol.% Fe_3C and ∼1200 με (for the (2 2 0)

reflection) for the present UHCS with 34 vol.% Fe_3C. In both cases, the α-Fe lattice strains increase only slightly up to sample failure, suggesting that once the α-Fe phase becomes plastic, failure is dependent upon the limitations of the ability of the Fe_3C phase to carry the load. In the case of the UHCS studied here, the maximum effective stress measured in the Fe_3C phase just before sample failure is ∼1630 MPa, which is close to ∼1730 MPa obtained just before sample failure in Ref. [35]. This result also suggests that the limiting feature of strain redistribution between phases is plasticity in the α-Fe around the Fe_3C particles, i.e. a larger volume fraction of Fe_3C leads to a larger reduction in the lattice strain in the α-Fe, but is limited by local plasticity and is not linearly correlated to volume fraction.

4.4. Anisotropy of lattice strains

In Fig. 8a, the α-Fe (2 2 0) reflection is compared in two orthogonal directions (ND and TD) relative to the rolling direction (RD, parallel to the applied stress). In the steel elastic range, no significant differences exist, whereas in the plastic range, load transfer from matrix to reinforcement is more pronounced in ND than in TD. This difference in load transfer is not due to α-Fe grain or Fe_3C particle shape, because these are all isotropic. This difference may be due to a gradient of deformation between the core and the surface of the rolled sheet resulting in different levels of plastic anisotropy in the two regions [72]. In the TD case, the X-ray beam samples only the core of the rolling plate, whereas for the ND case, the core as well as the front and back rolling surfaces are sampled, as shown in Fig. 8c. As illustrated in Fig. 4a and b, differences between the normal direction and the transverse direction were observed in the initial texture where the less stiff α-Fe (2 0 0) reflections were slightly more oriented in the normal direction and the stiffer (2 1 1) reflections were slightly less oriented in the normal direction, which further supports the possibility of a gradient of deformation between the core and the surface due to rolling. Stress equilibrium requires that the difference in load transfer present between ND and TD in α-Fe in the steel plastic range (Fig. 8a) produce a corresponding response in the Fe_3C curves (Fig. 8b). This effect is not observed in Fig. 8b in which the Fe_3C curves overlap in the steel plastic range, perhaps due to a lack of sufficient strain measurement resolution.

Fig. 9a illustrates microstructural anisotropic effects among the elastic load transfer behavior for the α-Fe (2 0 0) and the (2 2 0) and (2 1 1) reflections. Using the Kröner model [71] with elastic constants for α-Fe from Ref. [73] provides elastic moduli values ($E_{200} = 175$ GPa and $v = 0.33$; $E_{220/112} = 225$ GPa and $v = 0.28$) that are somewhat higher than, but probably within error of, experimental values ($E_{200} = 155$ GPa and $v = 0.33$; $E_{220/112} = 209/206$ GPa and $v = 0.28$). By contrast, all three (0 2 0), (2 2 0), and (1 1 2) Fe_3C reflections are approximately equivalent in the steel elastic range, suggesting that no elastic

anisotropic effects are present. However, in the steel plastic range, less load is carried by the Fe_3C (220) reflection than by the (020) and (112) reflections. A similar anisotropic Fe_3C response was reported by Kanie et al. [33] in the plastic range of a high-carbon steel. Assuming that the Fe_3C phase remains elastic in the steel plastic range, this anisotropic behavior is unexpected in view of the isotropic behavior in the elastic steel range. One possible explanation is that there is a crystallographic relationship between the two phases, so that the anisotropic behavior of the matrix is reflected in that of the Fe_3C.

By comparing the individual α-Fe reflections in Fig. 9a with data previously reported in Refs. [32–35], the elastic anisotropy is observed to be qualitatively in good agreement, with the (200) reflection most compliant. However, the diffraction data presented here have lower error bars, and the shorter count times allow for a much larger number of data points in the plastic range. Just after Lüders band propagation, the lattice strain observed for the α-Fe (200), (220) and (211) reflections are approximately equivalent. Upon further loading, the (220) and (211) reflections initially relax slightly more before increasing in strain up to failure. This behavior differs from the (200) reflection, where the strain gradually increases up to failure, leading to an overall larger magnitude of strain.

4.5. Residual strains

Unlike most MMCs [9–28,54–56], the present UHCS shows near-zero residual stresses after cooling from the processing temperature (Figs. 7–9). This can be explained by considering the two phenomena producing residual stresses in this composite: (i) the matrix/reinforcement mismatch in coefficients of thermal expansions, producing compressive strains in the cementite phase; and (ii) the allotropic γ–α transformation of the Fe matrix, producing tensile stresses in the cementite phase. The linear mismatch strain produced upon cooling from 727 to 20 °C because of the mismatch in thermal expansion values for α-Fe ($11.8 \times 10^{-6} K^{-1}$ [74]) and Fe_3C ($6.8 \times 10^{-6} K^{-1}$ [53]) is calculated as $-5 \times 10^{-6} \times 707 = -0.35\%$. This thermal contraction mismatch strain is exactly balanced by the linear mismatch strain due to the matrix allotropic expansion (0.35%) [75], thus explaining the observed near-zero residual strains. It should, however, be noted that the residual strains measured here come from the deviatoric strains rather than the hydrostatic strains. To determine the hydrostatic stresses, one can use stress-free powders (assuming these represent the true phases in the steel, as in Ref. [76]), or extract the two phases from steel of the same composition and heat-treatments to determine the exact contribution from the hydrostatic strains.

The slightly higher measured values of lattice parameters for both the α-Fe and Fe_3C phases as compared to the literature [52,53] may be within experimental error. It is also possible that it is a result of alloying additions,

which are known to influence the lattice parameters of both α-Fe and Fe_3C phases [53]: Mn and Cr partially replace Fe in Fe_3C and thus lead to a slightly larger lattice parameter for the Fe_3C phase, since both Mn and Cr are atomically slightly larger than Fe. Aluminum partitions to the α-Fe where it is in solid solution, and since Al is also atomically larger than Fe, this addition also leads to expansion of the lattice parameter for α-Fe.

Fig. 11a and b shows residual elastic strains for the Fe (200) and (220) reflections and the Fe_3C (220) and (112) reflections plotted against the macroscopic steel strain. As described by Oliver et al. [35], these residual elastic phase strains were calculated by subtracting the extrapolated linear elastic response from the non-linear plastic response under load (both shown in Fig. 7). These authors showed for a high-carbon steel with 1 wt.% C that this method gave residual strain values nearly identical to those measured directly after stress removal. In Fig. 11a and b, no residual strains are observed up to 0.33% macroscopic steel strain, as expected from the fact that both phases remain elastic during loading. During Lüders band propagation (0.33–1.1% steel strain), only a few data points were collected and residual phase strains remain near zero. After
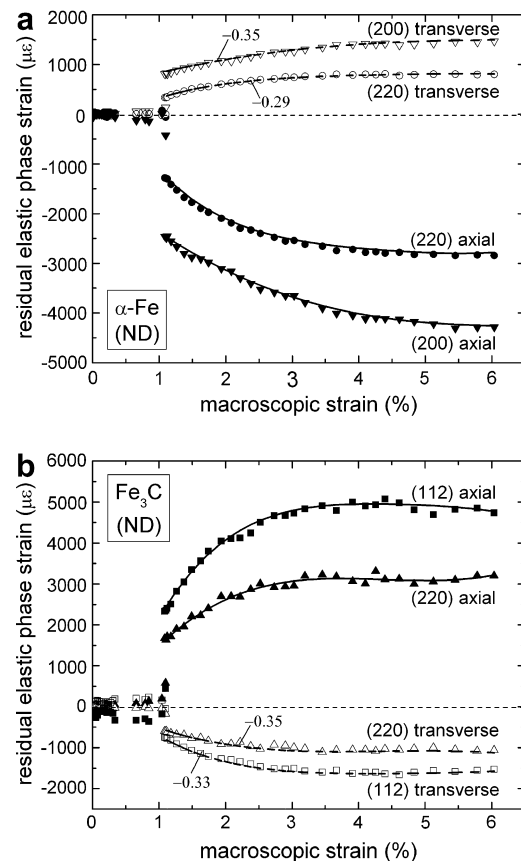

Fig. 11. Residual elastic phase strains in (a) α-Fe for (200) and (220) reflections and (b) Fe_3C for (220) and (112) reflections vs. macroscopic steel strain. The solid lines for the axial strains are best-fit curves through the data points. The dotted lines for the transverse strains are produced by multiplying the solid lines by a factor indicated next to the lines.

Lüders band propagation (>1.1% steel strain), the residual strains jump to a non-zero value and increase at an initially high rate until they saturate at a macroscopic steel strain of about 3%. While these results are qualitatively similar to those shown in Ref. [35], almost 10 times as many data points were collected in the present investigation, thus making the trend of increasing residual strain with plastic strain much more clearly visible. As suggested in Ref. [35], saturation occurs as a result of plastic relaxation of the matrix and suggests that the cementite is loaded elastically throughout the steel deformation and does not undergo plasticity, fracture or interfacial damage.

As pointed out by Oliver et al. [35], the ratio of the average axial to transverse residual strains should be $-1/2$ for each phase over the whole range of macroscopic deformation. This prediction holds for average phase strains, as determined using Rietveld refinement by Oliver et al. [35] for their high-carbon steel, but not necessarily for individual reflections, as examined here. Fitting the curves shown in Fig. 11a and b, this ratio is found to be approximately $-1/3$ for the α-Fe phase (with -0.35, -0.29 and -0.28 for the (200), (220) and (211) reflections, respectively) as well as the Fe_3C phase (with -0.34, -0.35, -0.33, -0.25, and -0.34 for the (020), (220), (112), (212), and (123) reflections, respectively).

4.6. Finite-element modeling

Finite-element modeling results for transverse and axial strains for both phases matched reasonably well with the experimental applied stress vs. lattice strain curves, as illustrated in Figs. 7–9. The model used average isotropic material properties, and cannot capture the anisotropic effects observed experimentally in Figs. 8 and 9. Nevertheless, it is encouraging that the model predicts axial strains falling between the measured (220) and (020)/(112) Fe_3C strains over the whole range of the steel deformation (Fig. 9b). Transverse lattice strains for the α-Fe in the steel plastic range are somewhat underpredicted (Fig. 9a), possibly due to systematic errors in the determination of the strain from the nonlinear lattice strain/lattice spacing vs. $\sin^2 \psi$ distribution curves (Fig. 6b). Two other important possible sources of error in the model are uncertainties in volume fraction of the two phases and the large-scale inhomogeneities observed in the steel (Fig. 3a). Other errors are imposed by the use of a unit cell approach, given that the Fe_3C particles are neither monosized nor distributed in a simple cubic lattice. It is also known that an aperiodic finite-element modeling approach for MMCs provides different stress-partitioning predictions to the periodic finite-element modeling approach used here [35,57,67,77–82]. Finally, the Cr and Mn content in the Fe_3C phase are unknown and hence so is their effect on the cementite elastic constants.

The finite-element results shown in Figs. 7–9 are spatially averaged for each phase, so these can be compared to the measured strains, which are averaged over the diffraction volume. Fig. 10a–c provides an illustration of the spatial variation of the effective stress in each phase. In Fig. 10a, where the steel is in the elastic range, the von Mises stress distribution is very uniform in both phases, as expected from the small mismatch in Young's moduli between the two phases (211 and 202 GPa for α-Fe and Fe_3C, respectively [32,53]) and the near-zero initial residual strains. After yielding, the von Mises stress (and therefore strain) distribution become spatially much less uniform (Fig. 10b): a steep stress gradient exists at the matrix/particle interface, and the stresses further increase in the center of the precipitate. While the average phase-effective stress are $\sigma_{\text{eff,ave,Fe}} = 418$ MPa and $\sigma_{\text{eff,ave,Fe3C}} = 974$ MPa, the highest stress in the matrix (near the particle) and in the particle (at its center) reach values of $\sigma_{\text{eff, max,Fe}} = 694$ MPa and $\sigma_{\text{eff, max,Fe3C}} = 1447$ MPa, respectively. This spatial anisotropy is further exacerbated at the maximum applied stress before failure (Fig. 10c): the phase average effective stresses ($\sigma_{\text{eff,ave,Fe}} = 461$ and $\sigma_{\text{eff,ave,Fe3C}} = 1626$ MPa), are much lower than their peak values ($\sigma_{\text{eff, max,Fe}} = 820$ and $\sigma_{\text{eff, max,Fe3C}} = 2925$ MPa). It is thus apparent that plastic load transfer from matrix to reinforcement leads not only to a disparity in average stresses between the phases (which can be measured by diffraction) but also to an increase in the spatial anisotropy of stress within each phase.

5. Conclusions

Synchrotron X-ray diffraction was used to study lattice strain evolution during tensile loading of a UHCS consisting of an α-Fe matrix containing 34 vol.% Fe_3C spheroidized particles about 1 μm in size. The following conclusions were reached:

1. Unlike ex situ MMCs with similar volume fractions of ceramic particles, no thermal residual stresses are observed in the UHCS. This is explained by the fact that the strain mismatches due to thermal expansion and allotropic transformation exactly counterbalance each other.
2. Also unlike ex situ composites, the UHCS shows no matrix/reinforcement load transfer in the elastic range of steel deformation, which is explained by a near exact match in elastic constants for the two phases. However, like ex situ composites, the UHCS exhibits marked load transfer from matrix to reinforcement in the plastic range of the steel, as expected if the plastically deforming matrix sheds load to the elastic reinforcement.
3. In the steel elastic range, no differences are observed between the two orthogonal directions relative to the rolling direction and the applied stress. However, in the plastic range, somewhat more matrix load transfer is observed in the normal direction, possibly due to a gradient of deformation between the core and the surface of the sample due to rolling. This gradient is also observed in the initial texture of the sample.

4. Microstructural anisotropic effects on load transfer are observed for both phases. For the α-Fe phase in the steel elastic range, the (200) reflection is less stiff than the (220) and (211) reflections; in the plastic range, less load transfer occurs for the (200) reflection than for the (220) and (211) reflections. For the Fe$_3$C phase, no anisotropic effects are present in the steel elastic range, while in the steel plastic range, more load is carried by the (020) and (112) reflections than by the (220) reflection.

5. Using a two-parameter fitted power-law hardening equation for the matrix, finite-element modeling was used to generate the macroscopic stress–strain curve. Despite its relative simplicity, the finite-element model provides a reasonable match with experimental diffraction strain data in both axial and transverse directions, for both α-Fe matrix and Fe$_3$C reinforcement, and over the whole elastic and plastic range of deformation of the steel.

Acknowledgements

References

[1] Sherby OD, Wadsworth J. J Mater Process Technol. 2001;117:347–53.
[2] Wadsworth J, Lesuer DR. Mater Charact 2000;45:289–313.
[3] Sherby OD, Wadsworth J. SAMPE J 1995;31:10–7.
[4] Taleff EM, Bramfitt BL, Syn CK, Lesuer DR, Wadsworth J, Sherby OD. Mater Charact 2001;46:11–8.
[5] Verhoeven JD, Pendray AH, Dauksch WE. JOM 1998;50:58–64.
[6] Verhoeven JD, Pendray AH. Mater Charact 1993;30:175–83.
[7] Verhoeven JD, Pendray AH, Berge PM. Mater Charact 1993;30:187–200.
[8] Mortensen A, Jin I. Int Mater Rev 1992;37(3):101–28.
[9] Daymond MR, Lund C, Bourke MAM, Dunand DC. Metall Mater Trans A-Phys Metall Mater Sci 1999;30(11):2989–97.
[10] Vaidyanathan R, Bourke MAM, Dunand DC. Acta Mater 1999;47(12):3353–66.
[11] Clausen B, Bourke MAM, Brown DW, Ustundag E. Mater Sci Eng A 2006;421:9–14.
[12] Allen AJ, Bourke MAM, Dawes S, Hutchings MT, Withers PJ. Acta Metall Mater 1992;40(9):2361–73.
[13] Withers PJ, Clarke AP. Acta Mater 1998;46(18):6585–98.
[14] Winand HMA, Whitehouse AF, Withers PJ. Mater Sci Eng A 2000;284:103–12.
[15] Dutta M, Bruno G, Edwards L, Fitzpatrick ME. Acta Mater 2004;52:3881–8.
[16] Hanan JC, Mahesh S, Ustundag E, Beyerlein IJ, Swift GA, Clausen B, et al. Mater Sci Eng A 2005;399:33–42.
[17] Shi N, Bourke MAM, Roberts JA, Allison JE. Metall Mater Trans A-Phys Metall Mater Sci 1997;28(12):2741–53.
[18] Madgwick A, Mori T, Withers PJ. Mater Sci Eng A 2002;333(1–2):232–8.
[19] Daymond MR, Fitzpatrick ME. Metall Mater Trans A 2006;37A(6):1977–86.
[20] Maire E, Owen A, Buffiere JY, Withers PJ. Acta Mater 2001;49(1):153–63.
[21] Preuss M, Rauchs G, Withers PJ, Maire E, Buffiere JY. Composit Part A-Appl Sci Manuf 2002;33(10):1381–5.
[22] Preuss M, Withers PJ, Maire E, Buffiere JY. Acta Mater 2002;50(12):3177–92.
[23] Sinclair R, Preuss M, Maire E, Buffiere J-Y, Bowen P, Withers PJ. Acta Mater 2004;52(6):1423–38.
[24] Balch DK, Ustundag E, Dunand DC. Metall Mater Trans A 2003;34(9):1787–97.
[25] Wanner A, Dunand DC. Metall Mater Trans A-Phys Metall Mater Sci 2000;31(11):2949–62.
[26] Korsunsky AM, James KE. Mater Sci Forum 2002;404(4):329–34.
[27] Pyzalla AR, Reetz B, Jacques A, Feiereisen JP, Ferry O, Buslaps T, et al. Z Metallkd 2004;95(7):624–30.
[28] Hanan JC, Ustundag E, Beyerlein IJ, Swift GA, Almer JD, Lienert U, et al. Acta Mater 2003;51(14):4239–50.
[29] Wilson DV, Bate PS. Acta Metall 1986;34(6):1107–20.
[30] Wilson DV, Konnan YA. Acta Metall 1964;12:617–28.
[31] Almer JD, Cohen JB, Winholtz RA. Metall Mater Trans A-Phys Metall Mater Sci 1998;29A:2127–36.
[32] Daymond MR, Priesmeyer HG. Acta Mater 2002;50(6):1613–26.
[33] Kanie A, Tomota Y, Torii S, Kamiyama T. ISIJ Int 2004;44(11):1952–6.
[34] Tomota Y, Suzuki T, Kanie A, Shiota Y, Uno M, Moriai A, et al. Acta Mater 2005;53:463–7.
[35] Oliver EC, Daymond MR, Withers PJ. Acta Mater 2004;52:1937–51.
[36] Balch DK, Ustundag E, Dunand DC. J Non-Cryst Solids 2003;317(1–2):176–80.
[37] Balch DK, Dunand DC. Acta Mater 2006;54(6):1501–11.
[38] Wanner A, Dunand DC. J Neutron Res 2002;10(1):57.
[39] Haeffner DR, Almer JD, Lienert U. Mater Sci Eng A 2005;399(1–2):120–7.
[40] Almer JD, Stock SR. J Struct Biol 2005;152(1):14–27.
[41] Almer JD, Lienert U, Peng RL, Schlauer C, Oden M. J Appl Phys 2003;94(1):697–702.
[42] Korsunsky AM, James KE, Daymond MR. Eng Fract Mech 2004;71(4–6):805–12.
[43] MATLAB. <www.mathworks.com>.
[44] Hammersley AP. ESRF97HA02T, FIT2D: An Introduction and Overview, ESRF Internal Report; 1997.
[45] Hammersley AP. ESRF98HA01T, FIT2D V9.129 Reference Manual V3.1, ESRF Internal Report; 1998.
[46] He BB, Smith KL. In: SEM spring conference on experimental and applied mechanics and experimental/numerical mechanics in electronic packaging III. TX: Houston; 1998.
[47] Wang YD, Lin Peng R, Wang X-L, McGreevy RL. Acta Mater 2002;50:1717–34.
[48] Wcislak L, Klein H, Bunge HJ, Garbe U, Tschentscher T, Schneider JR. J Appl Crystallogr 2002;35:82–95.
[49] Wenk H-R, Van Houtte P. Rep Prog Phy 2004;67:1367–428.
[50] Swanson HE et al. Natl Bur Stand (US) 1955;539(IV):3.
[51] Shimura S et al. Proc Jpn Acad 1930;6:269.
[52] Devers DJ. J Appl Phys 1972;43:3293–301.
[53] Umemoto M, Liu ZG, Masuyama K, Tsuchiya K. Scripta Mater 2001;45:391–7.
[54] Withers PJ, Bhadeshia HKDH. Mater Sci Technol 2001;17(4):355–65.
[55] Majumdar S, Singh JP, Kupperman D, Krawitz AD. J Eng Mat Tech 1991;113:51–9.
[56] Rangaswamy P, Prime MB, Daymond MR, Bourke MAM, Clausen B, Choo H, et al. Mater Sci Eng A 1999;259(2):209–19.

[57] Shen H, Lissenden CJ. Mater Sci Eng A 2002;338:271–81.
[58] Livescu V, Clausen B, Paggett JW, Krawitz AD, Drake EF, Bourke MAM. Mater Sci Eng A 2005;399:134–40.
[59] Gonzalez C, Llorca J. Acta Mater 2001;49:3505–19.
[60] Arsenault R, Shi N, Feng CR, Wang L. Mater Sci Eng A 1991;131:55–68.
[61] Christman T, Needleman A, Suresh S. Acta Metall 1989;37(11): 3029–50.
[62] Bush MB. Mater Sci Eng A 1992;154(2):139–48.
[63] Chawla N, Ganesh VV, Wunsch B. Scripta Mater 2004;51(2):161–5.
[64] Sorensen NJ, Suresh S, Tvergaard V, Needleman A. Mater Sci Eng A 1995;197(1):1–10.
[65] Saraev D, Schmauder S. Int J Plasticity 2003;19(6):733–47.
[66] Gonzalez C, Llorca J. Scripta Mater 1996;35(1):91–7.
[67] Weissenbeck E, Bohm HJ, Rammerstorfer FG. Comput Mater Sci 1994;3(2):263–78.
[68] Levy A, Papazian JM. Metall Mater Trans A 1990;21(2):411–20.
[69] Callister WD. Materials Science and Engineering. sixth ed. New York: Wiley; 2003.
[70] Hauk V, Nikolin HJ, Pintschovius L. Z Metallkd 1990;81:556–69.
[71] Noyan IC, Cohen JB. In: Ilschner B, Grant NJ, editors. Residual stress: measurement by diffraction and interpretation. New York: Springer; 1987.
[72] Johansson J, Oden M, Zeng X-H. Acta Mater 1999;47:2669–84.
[73] Hertzberg RW. Deformation and Fracture Mechanics of Engineering Materials. fourth ed. New York: Wiley; 1996.
[74] ASM Handbook Committee, Metals Handbook, 10th ed., vol. 2. Warrendale, PA: American Society for Metals; 1990.
[75] Basinski ZS, Hume-Rothery W, Sutton AL. Proc Roy Soc Lond 1955;A229:459.
[76] Hartmann S, Ruppersberg H. Mater Sci Eng A 2002;325:414–23.
[77] Borbely A, Biermann H, Hartmann O. Mater Sci Eng A 2001;313:34–45.
[78] Llorca J, Segurado J. Mater Sci Eng A 2003;365(1–2):267–74.
[79] Segurado J, Gonzalez C, Llorca J. Acta Mater 2003;51: 2355–69.
[80] Segurado J, Llorca J. J Mech Phys Solids 2002;50:2107–21.
[81] Mackerle J. Finite Elem Anal Des 2002;38(7):659–67.
[82] Mishnaevsky LL. Acta Mater 2004;52(14):4177–88.